

Constraining the Chiral Magnetic Effect in the heavy-ion collisions using AVFD model

Jagbir Singh^{1,2} Anjali Sharma^{1,3} Ankita Nain⁴ Madan M. Aggarwal¹

¹*Department of Physics, Panjab University Chandigarh 160014, India*

²*Present Address: Instituto de Alta Investigación, Universidad de Tarapacá, Casilla 7D, Arica 1000000, Chile*

³*Present Address: Department of Physical sciences, Bose Institute, Kolkata 700091, India*

⁴*Department of Physics, D.A.V. College, Sector 10, Chandigarh 160011, India*

E-mail: aggarwal@pu.ac.in

ABSTRACT: The Anomalous Viscous Fluid Dynamics (AVFD) framework is utilized to generate ${}^{197}_{79}\text{Au} + {}^{197}_{79}\text{Au}$, ${}^{96}_{44}\text{Ru} + {}^{96}_{44}\text{Ru}$, and ${}^{96}_{40}\text{Zr} + {}^{96}_{40}\text{Zr}$ collision events at $\sqrt{s_{\text{NN}}} = 200$ GeV, aiming to investigate the Chiral Magnetic Effect (CME). The CME signal is modulated through the axial charge per entropy density (n_5/s), varied as 0.0, 0.1, and 0.2 to produce distinct data sets with varying CME signal strengths. Additionally, a 33% local charge conservation (LCC) is implemented in each event. These data sets are analyzed using CME-sensitive two- and three-particle correlators. Furthermore, the Sliding Dumbbell Method (SDM) is employed to identify potential CME-like events within each data set. The identified events exhibit characteristics consistent with CME. The CME fraction in these events is quantified while accounting for backgrounds derived from charge shuffle events and correlated background contributions. No enhancement in the CME signal is observed in $\text{Ru} + \text{Ru}$ collisions compared to $\text{Zr} + \text{Zr}$ collisions, despite the presence of four additional protons in ${}^{96}_{44}\text{Ru}$ nuclei compared to ${}^{96}_{40}\text{Zr}$ nuclei.

KEYWORDS: Quark-Gluon plasma, chiral magnetic effect, charge separation, AVFD Model, sliding dumbbell method, 2- and 3- particle correlators

Contents

1	Introduction	1
2	Sliding Dumbbell Method	3
2.1	Background Estimation	4
3	Data Analyzed	4
4	Results and discussion	5
4.1	Analyzing data using Sliding Dumbbell Method	7
5	Summary	14

1 Introduction

Quantum chromodynamics (QCD) predicts that meta-stable domains with fluctuating topological charges can induce changes in the chirality of quarks, leading to local CP violation under conditions of extremely high temperatures and/or densities, such as those existed during quark-gluon plasma (QGP) formation [1–5]. In non-central heavy-ion collisions, the intense magnetic field generated by highly energetic spectator protons causes the separation of oppositely charged particles along the system’s angular momentum direction. This phenomenon is known as the Chiral Magnetic Effect (CME). The search for conclusive experimental evidence of the CME is a primary goal of the heavy-ion physics programs at both the Relativistic Heavy Ion Collider (RHIC) and the Large Hadron Collider (LHC). Such a discovery would have profound implications beyond heavy-ion physics, potentially marking a significant milestone in the field of physics as a whole. Consequently, extensive theoretical [6–12] and experimental [13–26] efforts have been devoted to probing the existence and properties of the CME. Number of methods [6, 27–30] have been proposed to detect the CME signal in heavy-ion collisions. Efforts have also been made to estimate the CME from the background using event shape engineering, pair invariant mass, etc. [31–35].

The Anomalous Viscous Fluid Dynamics (AVFD) framework [36–38] is introduced to simulate the evolution of chiral fermion currents in the Quark-Gluon Plasma (QGP) during heavy-ion collisions, build upon the VISHNU bulk hydrodynamic evolution. The AVFD model employs anomalous fluid dynamics to describe the development of fermion currents within the QGP, which forms as a result of these relativistic collisions. The underlying evolution of the bulk medium is described by VISH2+1 hydrodynamics [39], which provides a comprehensive view of the viscous behavior of the medium. The AVFD model integrates standard viscous hydrodynamics with anomalous fluid dynamics in a unified framework, considering crucial parameters such as initial conditions, magnetic fields,

and viscous transport coefficients. This integration allows for a dynamic interplay between the evolution of the axial charge current and the bulk medium. In the simulations, the EBE-AVFD Beta1.0 version of the model is utilized [34, 36]. The AVFD framework modulates the CME signal through the axial charge per entropy density (n_5/s), which reflects the imbalance between right-handed and left-handed fermions introduced during the initial stage of each event. Another critical parameter in the model is the percentage of local charge conservation (LCC) within an event, which influences the background by dictating the proportion of positively and negatively charged partners emitted from the same fluid element relative to the total event multiplicity.

The most widely used observable in the CME search is the “ γ -correlator,” originally proposed by Voloshin [6],

$$\gamma_{a,b} = \langle \cos(\phi_a + \phi_b - 2\Psi_{RP}) \rangle = \langle \cos(\Delta\phi_a)\cos(\Delta\phi_b) \rangle - \langle \sin(\Delta\phi_a)\sin(\Delta\phi_b) \rangle \quad (1.1)$$

where, ϕ_a and ϕ_b are azimuthal angles of particles a and b, respectively, and Ψ_{RP} represents the reaction plane angle. $\Delta\phi_a$ and $\Delta\phi_b$ represent the azimuthal angles measured with respect to the reaction plane. Here the averaging $\langle \cdot \cdot \cdot \rangle$ is performed over the pairs of particles and over events. We measure 3-particle γ -correlator which is equivalent to the above $\gamma_{a,b}$ and is defined as:

$$\gamma = \frac{\langle \cos(\phi_a + \phi_b - 2\phi_c) \rangle}{v_{2,c}} \quad (1.2)$$

where ϕ_a and ϕ_b , and ϕ_c represent azimuthal angles of particles. Here, a single particle “c” is used to measure the reaction plane angle and $v_{2,c}$ is the elliptic flow of particle c. In order to eliminate charge-independent correlation backgrounds mainly from global momentum conservation, the difference between the opposite-sign (OS) and same-sign (SS) γ -correlators is considered,

$$\Delta\gamma = \gamma_{OS} - \gamma_{SS} \quad (1.3)$$

The $\Delta\gamma$ is sensitive to the preferential emission of positively and negatively charged particles to the opposite sides of the reaction plane.

The reaction plane independent 2-particle δ -correlator is also used, which is as follows:

$$\delta_{a,b} = \langle \cos(\phi_a - \phi_b) \rangle = \langle \cos(\Delta\phi_a)\cos(\Delta\phi_b) \rangle + \langle \sin(\Delta\phi_a)\sin(\Delta\phi_b) \rangle \quad (1.4)$$

From equations 1.1 and 1.4, one can determine in-plane ($\langle \cos(\Delta\phi_a)\cos(\Delta\phi_b) \rangle$) and out-of-plane ($\langle \sin(\Delta\phi_a)\sin(\Delta\phi_b) \rangle$) correlations to certain the preferential emission of charged particles. Other methods to search for the CME signal are viz., R observable [27], participant and spectator planes method [28], signed balance function [29], and sliding dumbbell method [30].

In this analysis, the Sliding Dumbbell Method (SDM) [30] is employed to identify potential CME-like events. These events are further examined using the γ and δ correlators to confirm that they display the expected characteristics of CME events. Additionally, background contributions are meticulously addressed through the use of charge-shuffle and correlated backgrounds. The structure of this paper is as follows: section 2 provides a brief

overview of the SDM, followed by a discussion on background estimation in section 2.1. Section 3 presents various data samples utilized in this analysis, while results and discussion are given in section 4. Finally, a summary is provided in section 5.

2 Sliding Dumbbell Method

The ‘‘Sliding Dumbbell Method’’ (SDM) [30], has been developed to identify potential CME-like events those exhibit higher back-to-back charge separation on an event-by-event basis in heavy-ion collisions. This method is conceptually similar to the sliding window method used by the WA98 collaboration [40] to search for the disoriented chiral condensates. In the SDM, the azimuthal plane of each event is scanned by sliding a dumbbell-

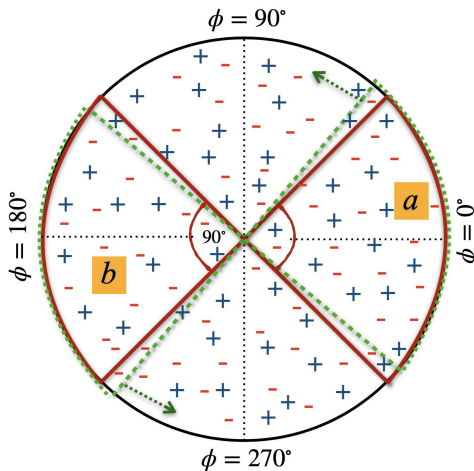


Figure 1. Pictorial representation of the transverse plane with hits of positive (+) and negative (-) charge particles in an event. The dumbbell is shown in solid red line while the slid dumbbell is shown in dotted green line.

shaped region with a size of $\Delta\phi = 90^\circ$ in steps of $\delta\phi = 1^\circ$ as shown in Fig. 1. This approach allows for the identification of the region with the maximum back-to-back charge separation. To quantify this separation, in this method we calculate Db_{+-} , which is the sum of the positive charge fraction on one side (‘‘a’’) of the dumbbell and the negative charge fraction on the other side (‘‘b’’) of the dumbbell, for each setting of the dumbbell across the azimuthal plane, i.e.,

$$Db_{+-} = \frac{n_a^+}{(n_a^+ + n_a^-)} + \frac{n_b^-}{(n_b^+ + n_b^-)} \quad (2.1)$$

where, $n_a^+(n_b^+)$ and $n_a^-(n_b^-)$ represent the number of positive and negative charged particles on sides ‘‘a’’ and ‘‘b’’ of the dumbbell, respectively. The $Db_{+-} = 2$ corresponds to 100% back-to-back charge separation while $Db_{+-} = 1$ means no back-to-back charge separation. Additionally, the charge excess asymmetry across the dumbbell, Db_{asy} , is defined as:

$$Db_{+-}^{asy} = \frac{(n_a^+ - n_a^-) - (n_b^- - n_b^+)}{(n_a^+ - n_a^-) + (n_b^- - n_b^+)} \quad (2.2)$$

Here, $n_a^+ - n_a^-$ represents the positive charge excess on the “a” side of the dumbbell whereas $(n_b^- - n_b^+)$ denotes the negative charge excess on the “b” side. From the 360 values obtained for both Db_{+-} and Db_{asy} by sliding the dumbbell in steps of $\delta\phi = 1^\circ$ across the azimuthal plane, the maximum value of Db_{+-} , termed Db_{+-}^{max} , is selected under the condition that $|Db_{asy}| < 0.25$. This constraint ensures the selection of CME-like events with balanced charge excess asymmetry. The charge separation across the dumbbell (f_{DbCS}) can be defined as:

$$f_{DbCS} = Db_{+-}^{max} - 1 \quad (2.3)$$

Hereafter, f_{DbCS} is referred as charge separation. For more details, please see ref. [30].

2.1 Background Estimation

To calculate the background contributions to the γ -correlator in different f_{DbCS} percentile bins (will be discussed in sec. 4.1) using the SDM, we consider contributions that might lead to higher charge separation purely by chance while maintaining the intrinsic correlations among particles. This is done by randomly shuffling the charges of particles in each event, keeping their momenta (i.e., θ and ϕ) unchanged. The charge-shuffle sample for a given centrality is then generated in the same way as the original data set [30]. The γ value for the charge-shuffle sample in a specific f_{DbCS} bin is referred to as γ_{Chs} . Meanwhile, the charge correlations those were disrupted by the charge shuffling are recovered from the original events corresponding to a given f_{DbCS} bins and termed as γ_{Corr} . Therefore, the total background contribution to the γ -correlator is expressed as:

$$\gamma_{Bkg} = \gamma_{Chs} + \gamma_{Corr} \quad (2.4)$$

This approach helps in estimating the background contribution to the γ -correlator.

3 Data Analyzed

The AVFD framework modulates the CME signal through the axial charge per entropy density (n_5/s), which reflects the imbalance between right-handed and left-handed fermions introduced during the initial stage of each event. The n_5/s parameter is varied, with values such as 0.0 (0%), 0.1 (10%), and 0.2 (20%) used as inputs to the AVFD simulations. Three

Table 1. Lists number of events analyzed for AVFD generated $Ru + Ru$, $Zr + Zr$, and $Au + Au$ collisions at $\sqrt{s_{NN}} = 200$ GeV for three different CME injections ($n_5/s = 0.0, 0.1, \text{ and } 0.2$), for 30–40% collision centrality.

AVFD (33% LCC)	$Au + Au$	$Ru + Ru$	$Zr + Zr$
$n_5/s = 0.0$	~95 M	~58 M	~48 M
$n_5/s = 0.1$	~58 M	~49 M	~71 M
$n_5/s = 0.2$	~77 M	~50 M	~56 M

different data sets are analyzed: $Au + Au$, $Ru + Ru$, and $Zr + Zr$ collisions at $\sqrt{s_{NN}} = 200$ GeV, each comprising three different samples based on varying levels of CME signal injection. All data samples for the 30-40% collision centrality include a 33% LCC, as detailed in Table 1.

4 Results and discussion

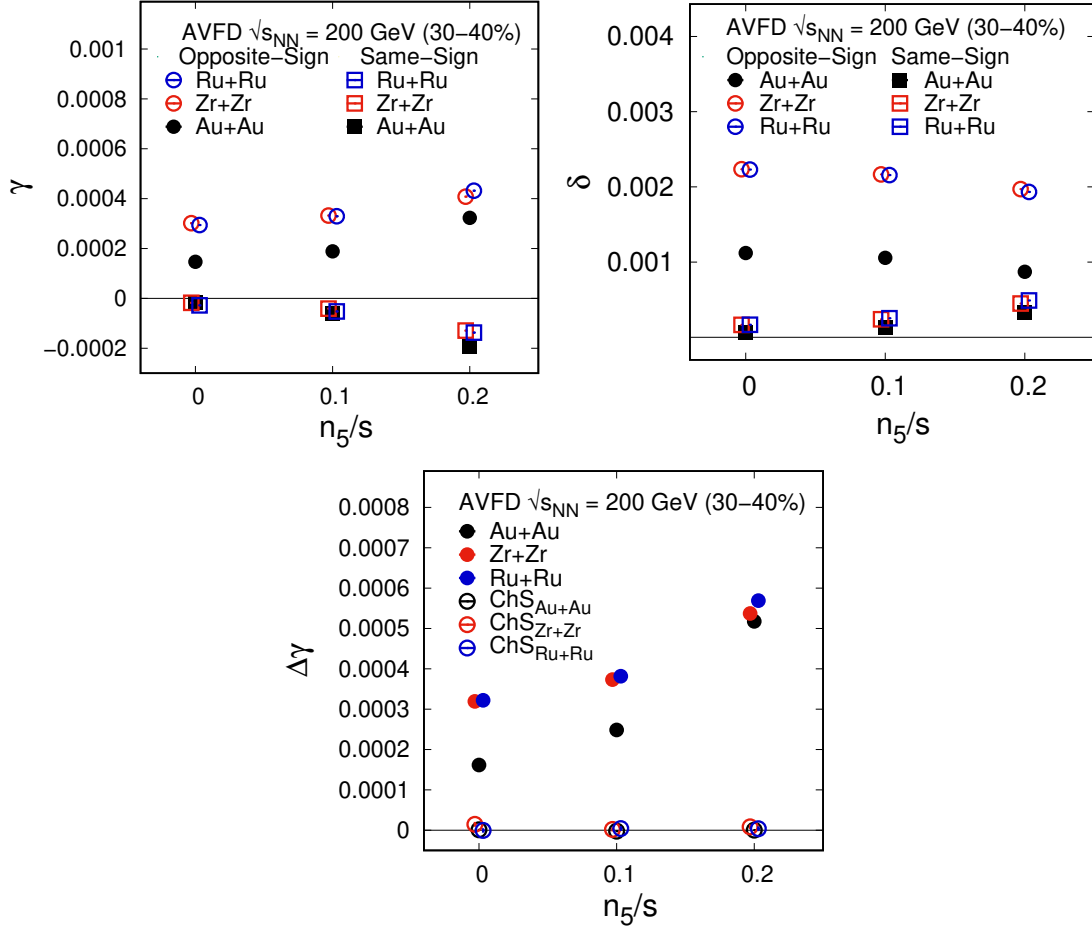


Figure 2. (Color Online) Three-particle γ -correlator (top left), two-particle δ -correlator (top right), and $\Delta\gamma$ (bottom) for AVFD generated $Ru + Ru$, $Zr + Zr$ and $Au + Au$ collisions at $\sqrt{s_{NN}} = 200$ GeV versus n_5/s ($= 0.0, 0.1,$ and 0.2) for 30-40% collision centrality. The $\Delta\gamma$ plot (bottom) also includes charge shuffle ($\Delta\gamma_{ChS}$) values. Markers are slightly shifted along the x-axis for clarity. Statistical uncertainties are small and are within the marker size.

Figure 2 (top left) shows the γ -correlator for opposite-sign (OS) and same-sign (SS) charge pairs in $Au + Au$ and isobar ($Ru + Ru$ and $Zr + Zr$) collisions at $\sqrt{s_{NN}} = 200$ GeV, with varying axial charge per entropy density ($n_5/s = 0.0, 0.1,$ and 0.2), all incorporating 33% local charge conservation (LCC). The results indicate that γ is negative for SS charge pairs and positive for OS charge pairs, with the magnitude of γ increasing as n_5/s increases from 0.0 to 0.2. Additionally, the γ values for the two isobar collisions ($Ru + Ru$ and

$Zr + Zr$) are similar within errors for both SS and OS charge pairs. Notably, γ is larger for OS pairs in isobar collisions compared to $Au + Au$ collisions, likely due to the increased background associated with the lower multiplicities in isobar collisions. The reaction plane independent δ -correlator for isobar and $Au + Au$ collisions and for different n_5/s values, is displayed in the Fig. 2 (top right). Both OS and SS charge pairs have positive δ values, but the OS pairs exhibit larger values. Again, it is observed that δ values are higher in isobar collisions compared to $Au + Au$ collisions, attributed to the increased background in the former. Figure 2 (Bottom) shows the dependence of the CME-sensitive $\Delta\gamma$ on n_5/s for isobar and $Au + Au$ collisions for 30-40% centrality. The data points at $n_5/s = 0.0$ show significant $\Delta\gamma$ values, despite the expectation of near-zero values in the absence of a CME signal. This anomaly is due to 33% LCC, which mimics a CME signal. However, in AMPT generated Au+Au collisions at $\sqrt{s_{NN}} = 200$ GeV without a CME signal, $\Delta\gamma$ was found to be approximately zero [30]. The $\Delta\gamma$ at $n_5/s = 0$ is almost twice in isobar collisions compared to $Au + Au$ collisions which scales inversely with multiplicities [41]. The multiplicities in isobar collisions are approximately half compared to $Au + Au$ collisions. The relative increase in $\Delta\gamma$ from $n_5/s = 0$ to $n_5/s = 0.1$ and 0.2 is more pronounced in $Au + Au$ collisions than in isobar collisions.

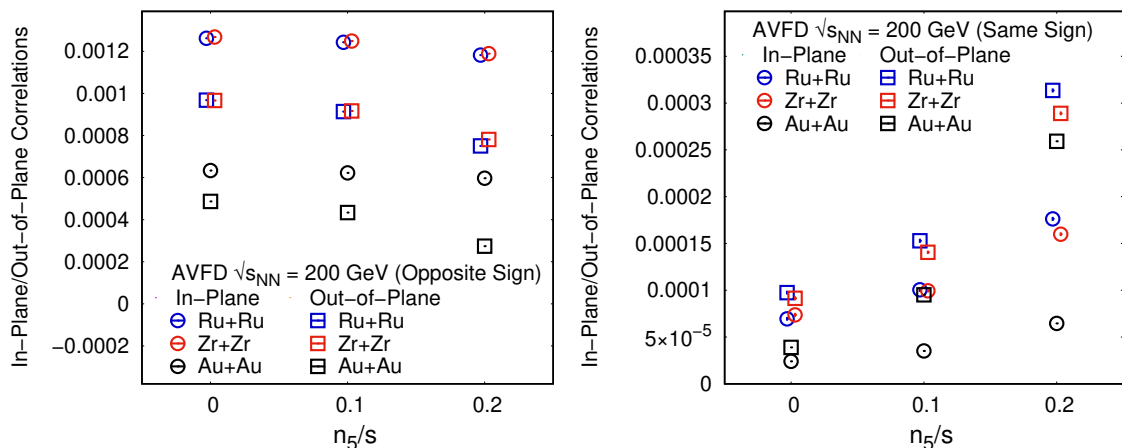


Figure 3. (Color Online) In-plane and out-of-plane correlations for opposite sign (left) and same sign (right) charge pairs for AVFD generated $Ru + Ru$, $Zr + Zr$, and $Au + Au$ collisions at $\sqrt{s_{NN}} = 200$ GeV for three different CME injections i.e., $n_5/s = 0.0, 0.1,$ and 0.2 , for the 30-40% collision centrality. Markers are slightly shifted along the x-axis for clarity. Statistical uncertainties are small and are within the marker size.

In-plane and out-of-plane correlations for the opposite- and same-sign charged pairs are displayed, respectively, in Fig. 3 (left) and Fig. 3 (right). Both in-plane and out-of-plane correlations are found to be positive for both OS and SS charge pairs, with OS pairs showing stronger in-plane correlations, while SS pairs exhibit stronger out-of-plane correlations.

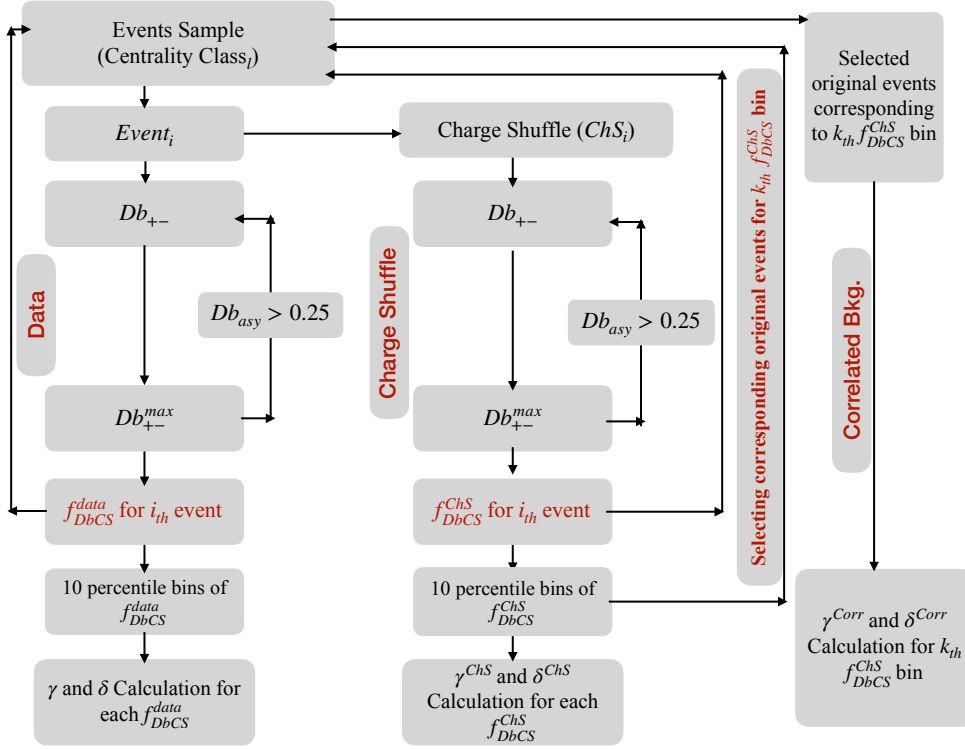


Figure 4. (Color Online) Flow chart displaying various steps involved in computing γ and δ correlators employing SDM.

4.1 Analyzing data using Sliding Dumbbell Method

Figure 4 displays the flow chart describing the various steps involved in the analysis as discussed in sections 2 and 3. In the initial phase of the analysis, the entire azimuthal plane of each event is scanned, and the f_{DbCS} distributions are computed for the 30–40% collision centrality and for different data sets. These distributions are subsequently categorized into ten percentile bins, ranging from 0–10% (representing the highest charge separation) to 90–100% (representing the lowest charge separation) for 30–40% collision centrality. Following this, multi-particle correlators (2-, 3-, and 4-particle) are calculated for each f_{DbCS} bin within a centrality class (i.e., 30–40%), utilizing samples from AVFD, charge shuffle, and correlated backgrounds.

The f_{DbCS} distributions for $Au + Au$ and $Ru + Ru$ collisions at $\sqrt{s_{NN}} = 200$ GeV for the 30–40% collision centrality, corresponding to different axial charge per entropy densities (n_5/s), along with charge shuffle (ChS) event sample, are shown in Fig. 5 (left) and Fig. 5 (right), respectively. These distributions show slight forward shift along with decreasing peak with increasing n_5/s values. Furthermore, the f_{DbCS} distributions for the charge shuffle across the various n_5/s values are nearly indistinguishable, so only distribution for $n_5/s = 0.2$ is shown. For $Zr + Zr$ collisions, distributions similar to $Ru + Ru$ collisions have been observed. After obtaining these f_{DbCS} distributions for $Au + Au$, $Ru + Ru$, and $Zr + Zr$ along with their corresponding ChS, these distributions are divided into 10

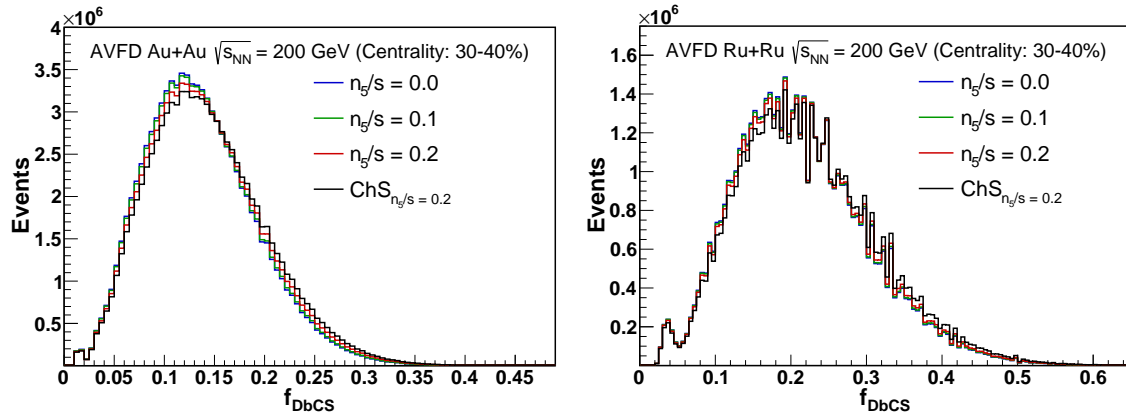


Figure 5. f_{DbCS} distributions for AVFD generated $Au+Au$ (left) and $Ru+Ru$ (right) collisions at $\sqrt{s_{NN}} = 200$ GeV for 30-40% collision centrality. The rightmost side of the distribution represents the highest charge separation (0-10% f_{DbCS}) and the leftmost side of the distribution represents the lowest charge separation (90-100% f_{DbCS}).

percentile bins as discussed above. This method of partitioning events based on f_{DbCS} helps identify potential CME-like events characterized by the highest back-to-back charge separation across the dumbbell.

Figure 6 displays the γ -correlator for opposite-sign (left) and same-sign (right) charge pairs as a function of f_{DbCS} percentile bins for $Ru+Ru$ (top), $Zr+Zr$ (middle), and $Au+Au$ (bottom) collisions. The comparison to charge shuffle (ChS) and correlated backgrounds (Corr bkg) are also shown. The magnitude of the γ -correlator increases for both same-sign (SS) and opposite-sign (OS) charge pairs in the higher f_{DbCS} bins, peaking in the top 10% f_{DbCS} bin. Within each f_{DbCS} bin, the correlation is strongest for $n_5/s = 0.2$ and progressively weaker for $n_5/s = 0.1$ and 0.0 , indicating a direct relationship between the CME signal injection and the γ -correlator. For the SS pairs, the γ -correlator is negative in the top f_{DbCS} bins, but becomes positive for lower f_{DbCS} bins, suggesting a trend toward normal events as f_{DbCS} decreases. The γ -correlator values are significantly higher in top f_{DbCS} bins than the average centrality values, indicating a strong CME signal in the top f_{DbCS} bins. The γ -correlator for both SS and OS pairs in the charge shuffle (ChS) background increases significantly in the top f_{DbCS} bins and remains approximately constant within each f_{DbCS} bin across all AVFD sets, regardless of the CME signal strength. The γ -correlator for the correlated background is consistent across all f_{DbCS} bins for each AVFD set, with the highest values observed for $n_5/s = 0.2$. The γ -correlator for $Ru+Ru$ and $Zr+Zr$ collisions shows higher correlations compared to $Au+Au$ collisions, as seen in Fig. 6, primarily due to increased background in the isobaric collisions. Notably, for the top 20% f_{DbCS} bins, the magnitude of $|\gamma_{SS}|$ is approximately equal to $|\gamma_{OS}|$ across all data sets for $Ru+Ru$, $Zr+Zr$, and $Au+Au$ collisions, including their charge shuffle events. This behavior is distinct from what is observed in Fig. 2, which represents the overall centrality.

Two-particle δ correlators for $n_5/s = 0.0, 0.1,$ and 0.2 for $Ru+Ru$ (top left), $Zr+Zr$

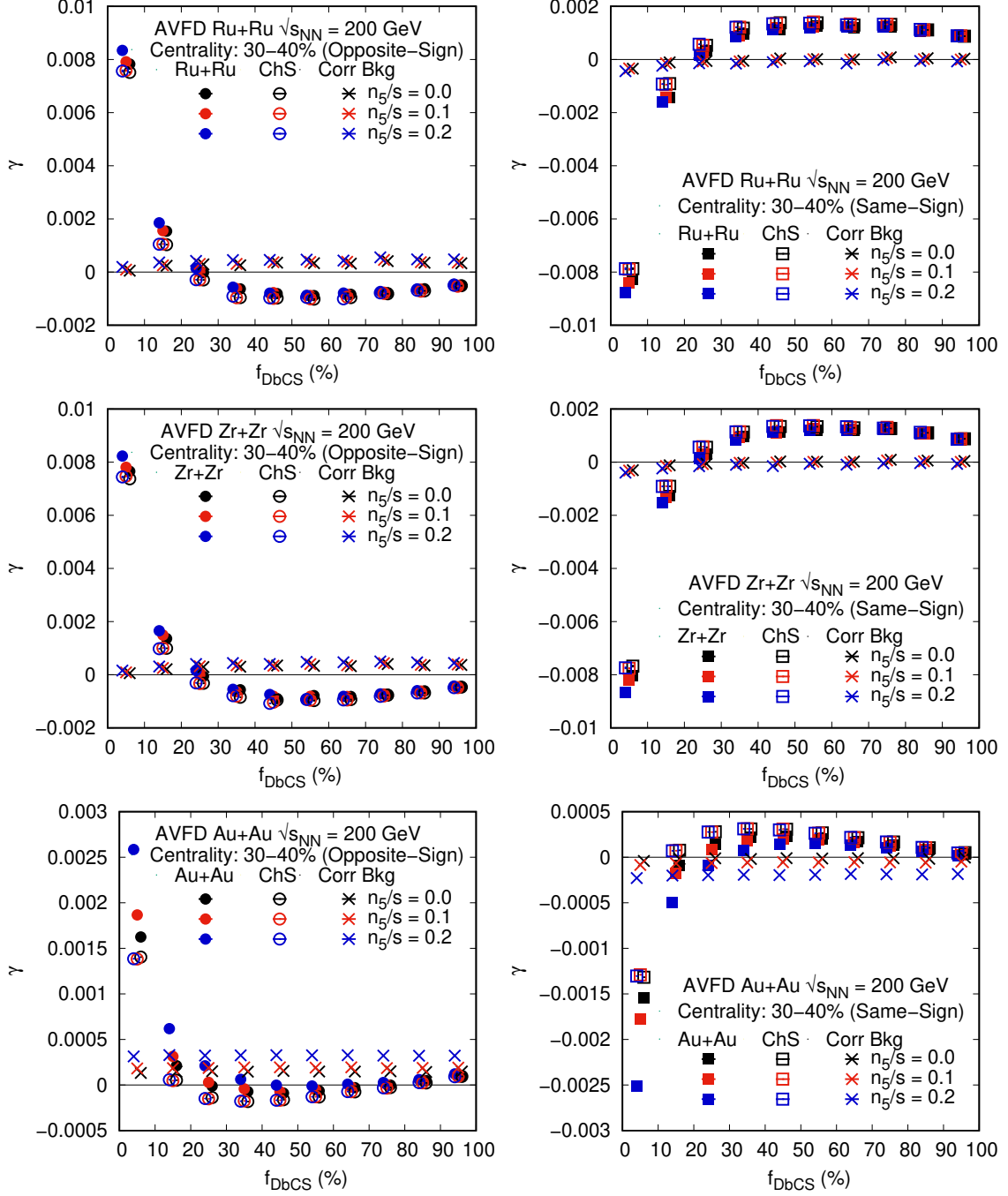


Figure 6. (Color online) γ -correlator as a function of f_{DbCS} for $Ru + Ru$, $Zr + Zr$ and $Au + Au$ collisions at $\sqrt{s_{NN}} = 200$ GeV for opposite-sign (Left) and same-sign (Right), for three different CME samples i.e., $n_5/s = 0.0, 0.1,$ and 0.2 , for 30-40% collision centrality. γ -correlator for charge-shuffle background (γ_{ChS}) and correlated background (γ_{Corr}) is also shown in the figure. The markers are slightly shifted along the x-axis for clarity. Statistical uncertainties are small and are within the marker size.

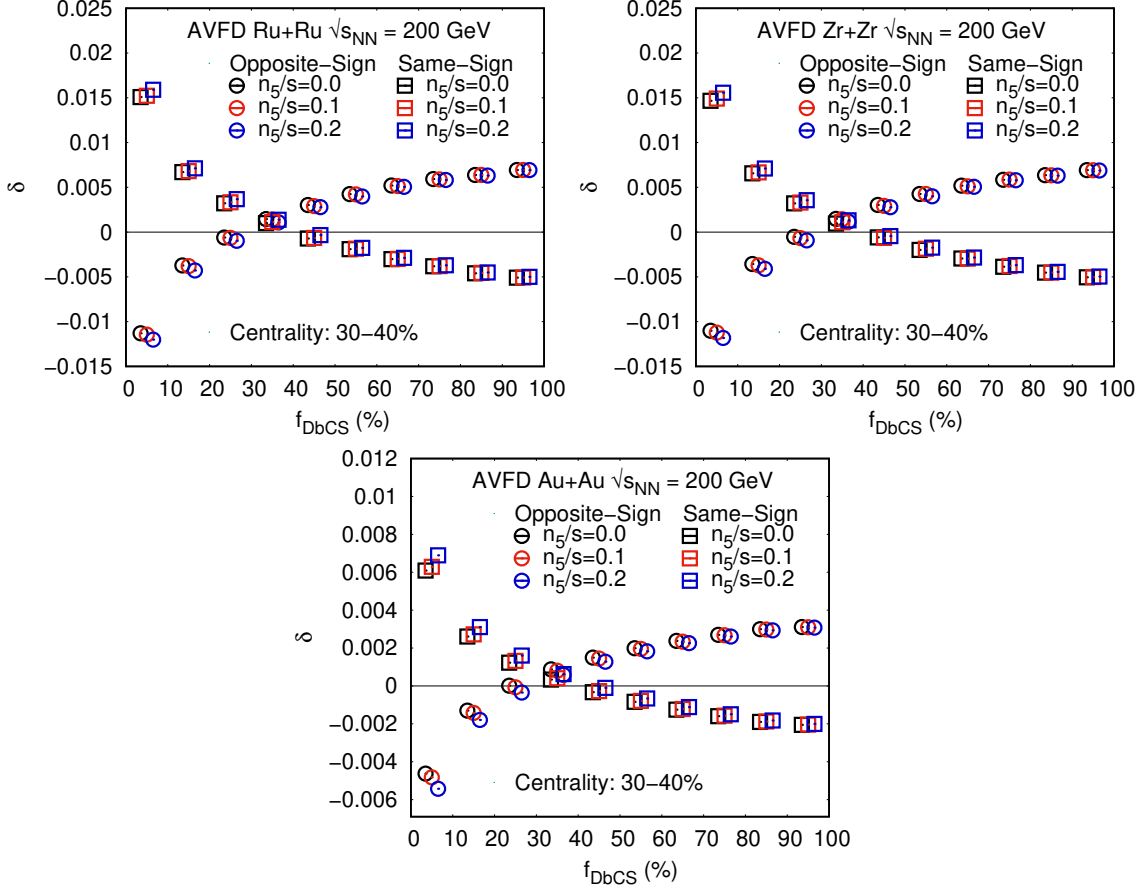


Figure 7. (Color online) δ -correlator as a function of f_{DbCS} for $Ru + Ru$, $Zr + Zr$ and $Au + Au$ collisions at $\sqrt{s_{NN}} = 200$ GeV for opposite-sign and same-sign, for three different CME samples i.e., $n_5/s = 0.0, 0.1,$ and 0.2 , for 30-40% collision centrality. Markers are slightly shifted along the x-axis for clarity. Statistical uncertainties are small and are within the marker size.

(top right), and $Au + Au$ (bottom) collisions, focusing on both opposite-sign and same-sign charged particles are presented in Fig. 7. The results indicate that δ_{OS} is negative while δ_{SS} is positive for the top 20% f_{DbCS} bins. This is in contrast to the three-particle correlators, where γ_{OS} is positive and γ_{SS} is negative, which aligns with expectations for CME-like events in the top 20% f_{DbCS} bins [7]. Additionally, the δ correlator shows a weak dependence on n_5/s .

Figure 8 displays the in-plane and out-of-plane correlations for $Ru + Ru$ (top), $Zr + Zr$ (middle), and $Au + Au$ (bottom) collisions at $\sqrt{s_{NN}} = 200$ GeV, with axial charge density per entropy $n_5/s = 0.0, 0.1,$ and 0.2 , for opposite-sign (left) and same-sign (right) charge pairs. The data reveals that opposite-sign correlations are stronger in the out-of-plane configuration, while in-plane correlations are weaker and show negative values in the top 20% f_{DbCS} bins across all three collision types. Conversely, same-sign correlations are positive and demonstrate stronger out-of-plane correlations compared to in-plane correlations within the top 20% f_{DbCS} bins. Furthermore, the out-of-plane correlations appear to

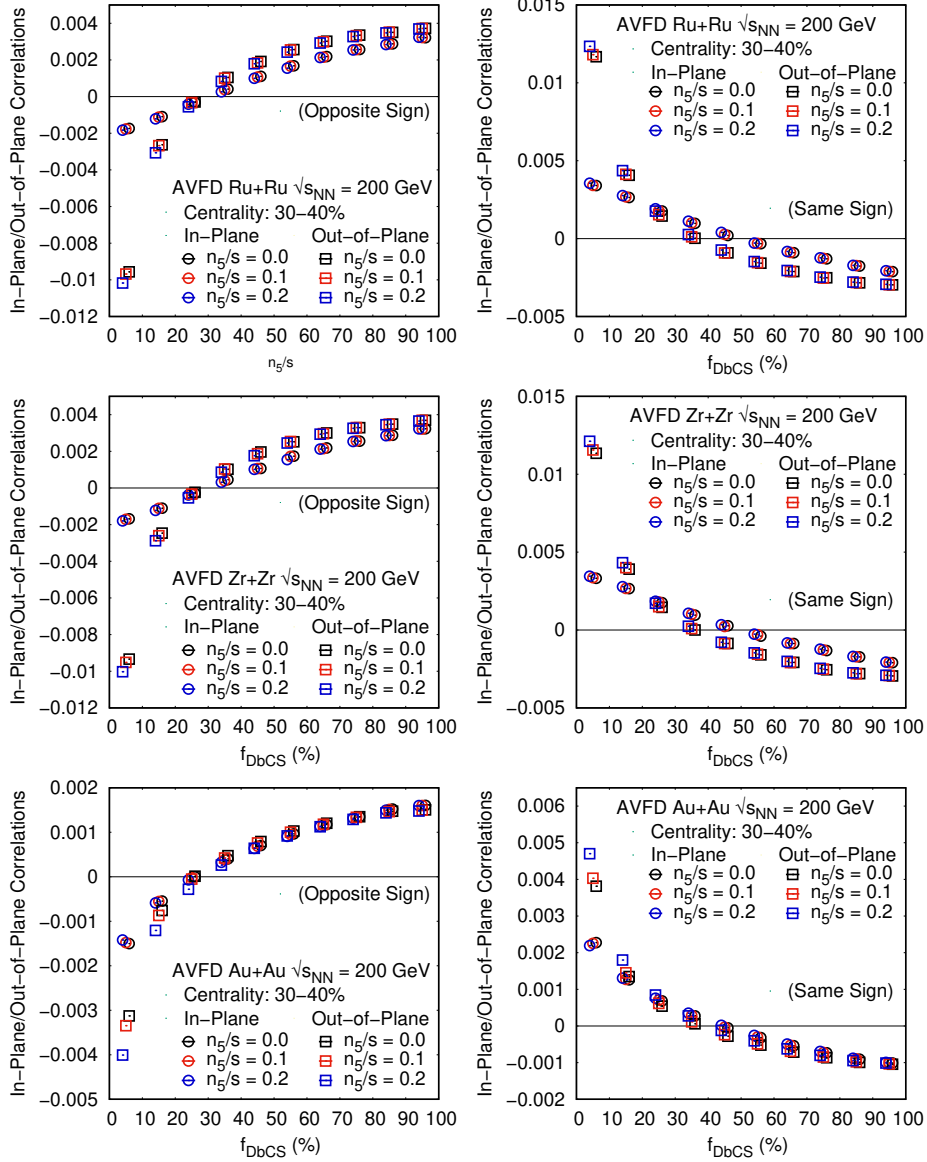


Figure 8. (Color online) In-plane and out-of-plane correlator as a function of f_{DbCS} for $Ru + Ru$, $Zr + Zr$ and $Au + Au$ collisions at $\sqrt{s_{NN}} = 200$ GeV for opposite-sign (Left) and same-sign (Right), for three different CME samples i.e., $n_5/s = 0.0, 0.1$, and 0.2 , for 30-40% collision centrality. Markers are slightly shifted along the x-axis for clarity. Statistical uncertainties are small and are within the marker size.

increase with rising axial charge density per entropy.

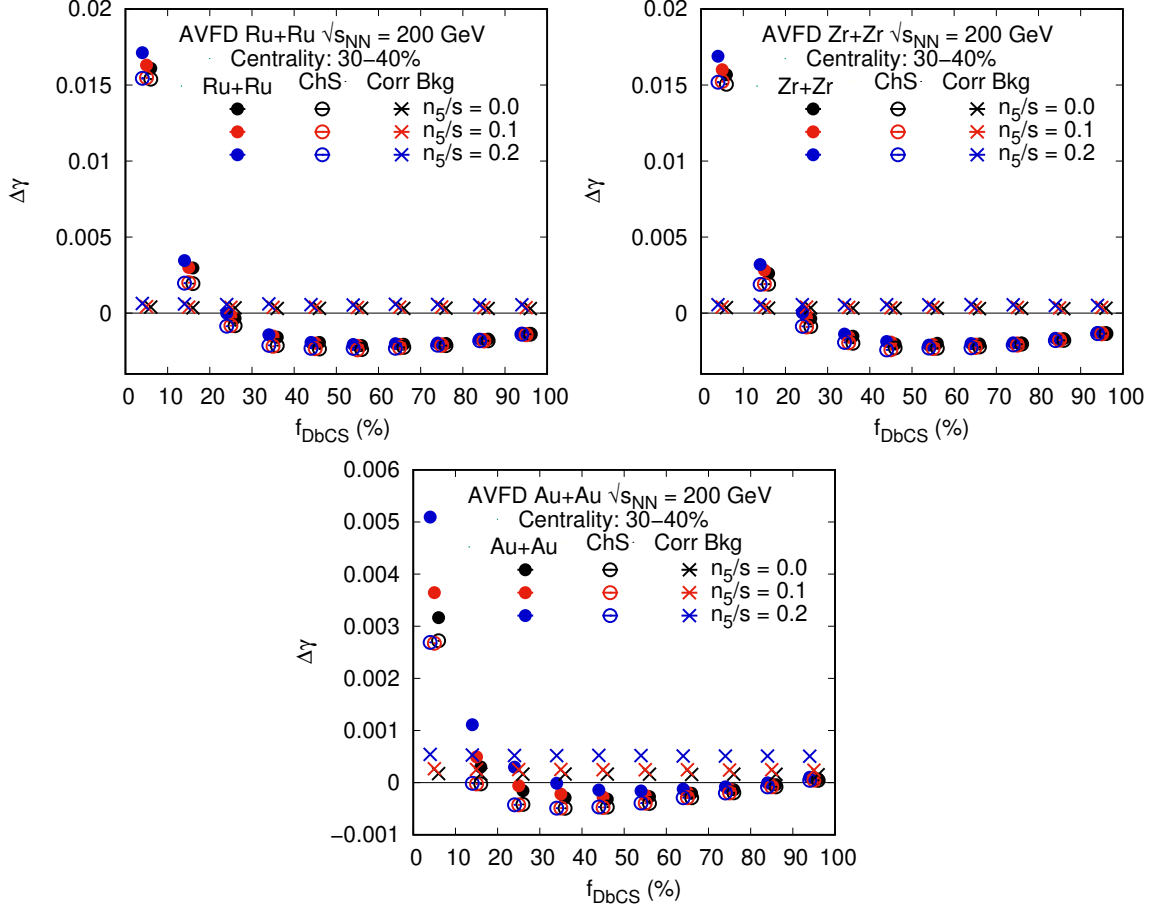


Figure 9. (Color online) $\Delta\gamma$ ($=\gamma_{OS}-\gamma_{SS}$) as a function of f_{DbCS} for AVFD generated $Ru + Ru$ (top left), $Zr + Zr$ (top right) and $Au + Au$ (bottom) collisions at $\sqrt{s_{NN}} = 200$ GeV, for three different CME samples i.e., $n_5/s = 0.0, 0.1,$ and 0.2 , for 30-40% collision centrality. $\Delta\gamma$ for charge shuffle background (γ_{ChS}) and correlated background (γ_{Corr}) are also displayed in the figure as open circles and cross markers, respectively, for $n_5/s = 0.0, 0.1,$ and 0.2 . Markers are slightly shifted along the x-axis for clarity. Statistical uncertainties are small and are within the marker size.

The $\Delta\gamma$ ($=\gamma_{OS}-\gamma_{SS}$) plotted against different f_{DbCS} percentile bins for $Ru + Ru$ (top left), $Zr + Zr$ (top right), and $Au + Au$ (bottom) collisions at $\sqrt{s_{NN}} = 200$ GeV are displayed in Fig. 9. Each plot includes results for different CME injected samples, represented by $n_5/s = 0.0, 0.1,$ and 0.2 , along with their corresponding charge shuffle (ChS) and correlated backgrounds (Corr bkg). As the CME signal increases, the $\Delta\gamma$ values rise across all f_{DbCS} bins. The highest $\Delta\gamma$ values are found in the top 10% f_{DbCS} bin, with values decreasing as f_{DbCS} decreases. The $\Delta\gamma$ values for ChS backgrounds are nearly identical within statistical errors as expected across all three sets of AVFD simulations with $n_5/s = 0.0, 0.1,$ and 0.2 . These values are lower than the actual data for $Ru + Ru, Zr + Zr,$ and $Au + Au$ collisions in top f_{DbCS} bins. The $\Delta\gamma$ values for the correlated backgrounds remain consistent across

all f_{D_bCS} bins, showing no significant variation. The $\Delta\gamma$ is generally higher in isobaric collisions ($Ru + Ru$ and $Zr + Zr$) compared to $Au + Au$ collisions. This is attributed to the fact that $\Delta\gamma$ varies inversely with multiplicity [41], which is higher in $Au + Au$ collisions, leading to lower $\Delta\gamma$ values. Additionally, it has been noted that $\Delta\gamma$ for the top 10% f_{D_bCS} bin is roughly ten times greater than the values observed for the overall centrality, as shown in Fig. 2 (bottom) across all data sets. This enhancement in top f_{D_bCS} bins is also reflected in the charge shuffle samples that represent background, although their values are nearly zero for overall centrality as shown in Fig. 2 (bottom).

Based on the above observations concerning the three-particle correlator (γ), two-particle correlator (δ), and in-/out-of-plane correlations, the top 20% of f_{D_bCS} events, which align with the expected CME signal [7], can be identified as potential CME candidates. Consequently, the fraction of CME (f_{CME}) can be calculated using the following equation:

$$f_{CME} = 1 - \frac{\Delta\gamma_{Bkg}}{\Delta\gamma_{AVFD}} \quad (4.1)$$

$$\Delta\gamma_{Bkg} = \Delta\gamma_{ChS} + \Delta\gamma_{Corr}$$

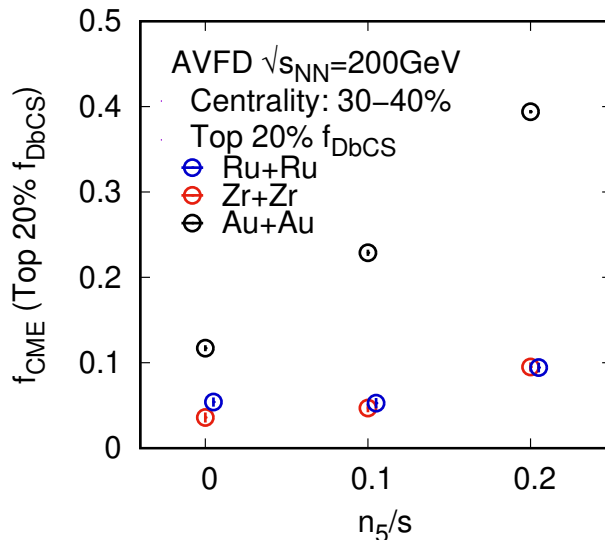


Figure 10. (Color online) f_{CME} versus n_5/s ($= 0.0, 0.1,$ and 0.2) for AVFD generated $Ru + Ru$, $Zr + Zr$ and $Au + Au$ collisions at $\sqrt{s_{NN}} = 200$ GeV for top 20% f_{D_bCS} bins for 30-40% collision centrality. Markers are slightly shifted along the x-axis for clarity. Statistical uncertainties are small and are within the marker size.

Figure 10 shows the fraction of CME (f_{CME}) as a function of n_5/s for $Au+Au$, $Ru+Ru$, and $Zr+Zr$ collisions. The results indicate that f_{CME} increases with increasing externally injected CME signal. For $Au + Au$ collisions, f_{CME} increases from approximately 11.5% at $n_5/s = 0.0$ to around 39% at $n_5/s = 0.2$, considering the top 20% f_{D_bCS} bins. In the $Ru + Ru$ collisions, f_{CME} increases from about 5% at $n_5/s = 0.0$ to approximately 9.5% at $n_5/s=0.2$. Similarly, for $Zr + Zr$ collisions, f_{CME} rises from approximately 3.6% at $n_5/s = 0.0$ to around 9.4% at $n_5/s = 0.2$. Notably, even at $n_5/s = 0.0$, f_{CME} exhibits positive

values. This suggests that the presence of 33% local charge conservation (LCC) in these samples mimics CME. For $n_5/s = 0.2$, the f_{CME} for $Au + Au$ collisions is approximately 39%, which is roughly four times larger than the values for $Ru + Ru$ and $Zr + Zr$ collisions.

It is observed that in $Au + Au$ collisions, the f_{CME} value doubles when n_5/s increases from 0.0 to 0.1, and triples when n_5/s reaches 0.2. However, in the case of isobaric collisions ($Ru + Ru$ and $Zr + Zr$), the increase in f_{CME} is less pronounced. Notably, there is no increase in f_{CME} when n_5/s changes from 0.0 to 0.1 in isobaric collisions. The small CME signal is difficult to distinguish in the presence of 33% LCC, as the background increases with decreasing multiplicity. Additionally, the results for $Ru + Ru$ and $Zr + Zr$ collisions are consistent within statistical errors. This consistency suggests that the increased magnetic field in $Ru + Ru$ collisions, compared to $Zr + Zr$, does not lead to a significant increase in the CME signal, consistent with experimental observations [23].

5 Summary

The AVFD model generated $^{197}_{79}Au + ^{197}_{79}Au$ and isobaric ($^{96}_{44}Ru + ^{96}_{44}Ru$ and $^{96}_{40}Zr + ^{96}_{40}Zr$) collisions, which contain varying CME signals with a fixed 33% LCC, have been extensively analyzed using sliding dumbbell method (SDM). The potential CME-like events identified through this method underwent scrutiny to ensure they exhibit the characteristics typical of CME events.

It was observed that the 33% LCC in the given samples mimics a CME-like signal. However, in $Au + Au$ collisions, a clear CME signal is detected in samples with CME signal exceeding 33% LCC, and this signal increases with increasing CME contribution. In contrast, such a trend is not evident in isobaric collisions, likely due to lower event multiplicities leading to significant background noise in these cases. Nevertheless, we do observe CME signals in samples with substantial injected CME; however, no differences in the CME signals between the two isobars are noted, consistent with previous experimental findings. Therefore, the absence of an enhanced CME signal in $Ru + Ru$ collisions compared to $Zr + Zr$ collisions in experiments should not be interpreted as evidence that CME does not exist. This is clearly illustrated by the AVFD model, which incorporates the CME signal and shows no increase in the CME signal for $Ru + Ru$ collisions over $Zr + Zr$ collisions.

The SDM can be applied to experimental data on $Au + Au$, $Ru + Ru$, $Zr + Zr$, and $Pb + Pb$ collisions to validate the CME signal, as it enables the identification of potential candidates with a significantly higher CME fraction compared to the conventional approach of searching within a fixed centrality range.

Acknowledgments

The authors sincerely thank Dr. Yufu Lin for generating and providing access to the AVFD events. The financial assistance from Department of Science & Technology, University Grants Commission, and Council of Scientific & Industrial Research, Government of India,

is gratefully acknowledged. The authors are also thankful to the Panjab University and the Department of Physics for providing an academic environment and research facilities.

References

- [1] D. Kharzeev, R.D. Pisarski and M.H.G. Tytgat, *Possibility of spontaneous parity violation in hot qcd*, *Phys. Rev. Lett.* **81** (1998) 512.
- [2] D. Kharzeev, *Parity violation in hot qcd: Why it can happen, and how to look for it*, *Physics Letters B* **633** (2006) 260.
- [3] D. Kharzeev and A. Zhitnitsky, *Charge separation induced by p-odd bubbles in qcd matter*, *Nuclear Physics A* **797** (2007) 67.
- [4] D.E. Kharzeev, L.D. McLerran and H.J. Warringa, *The effects of topological charge change in heavy ion collisions: “event by event and violation”*, *Nuclear Physics A* **803** (2008) 227.
- [5] K. Fukushima, D.E. Kharzeev and H.J. Warringa, *Chiral magnetic effect*, *Phys. Rev. D* **78** (2008) 074033.
- [6] S.A. Voloshin, *Parity violation in hot qcd: How to detect it*, *Phys. Rev. C* **70** (2004) 057901.
- [7] A. Bzdak, V. Koch and J. Liao, *Charge-dependent correlations in relativistic heavy ion collisions and the chiral magnetic effect*, in *Strongly Interacting Matter in Magnetic Fields*, D. Kharzeev, K. Landsteiner, A. Schmitt and H.-U. Yee, eds., (Berlin, Heidelberg), pp. 503–536, Springer Berlin Heidelberg (2013), DOI.
- [8] D. Kharzeev, J. Liao, S. Voloshin and G. Wang, *Chiral magnetic and vortical effects in high-energy nuclear collisions—a status report*, *Progress in Particle and Nuclear Physics* **88** (2016) 1.
- [9] V. Koch, S. Schlichting, V. Skokov, P. Sorensen, J. Thomas, S. Voloshin et al., *Status of the chiral magnetic effect and collisions of isobars*, *Chinese Physics C* **41** (2017) 072001.
- [10] B. Schenke, C. Shen and P. Tribedy, *Multiparticle and charge-dependent azimuthal correlations in heavy-ion collisions at the relativistic heavy-ion collider*, *Phys. Rev. C* **99** (2019) 044908.
- [11] J. Zhao and F. Wang, *Experimental searches for the chiral magnetic effect in heavy-ion collisions*, *Progress in Particle and Nuclear Physics* **107** (2019) 200.
- [12] K. Xu, S. Shi, H. Zhang, D. Hou, J. Liao and M. Huang, *Extracting the magnitude of magnetic field at freeze-out in heavy-ion collisions*, *Physics Letters B* **809** (2020) 135706.
- [13] W. Li and G. Wang, *Chiral magnetic effects in nuclear collisions*, *Annual Review of Nuclear and Particle Science* **70** (2020) 293.
- [14] STAR collaboration, *Azimuthal charged-particle correlations and possible local strong parity violation*, *Phys. Rev. Lett.* **103** (2009) 251601.
- [15] STAR collaboration, *Observation of charge-dependent azimuthal correlations and possible local strong parity violation in heavy-ion collisions*, *Phys. Rev. C* **81** (2010) 054908.
- [16] STAR collaboration, *Fluctuations of charge separation perpendicular to the event plane and local parity violation in $\sqrt{s_{NN}} = 200$ GeV Au+Au collisions at the BNL Relativistic Heavy Ion Collider*, *Phys. Rev. C* **88** (2013) 064911.

- [17] STAR collaboration, *Beam-energy dependence of charge separation along the magnetic field in Au+Au collisions at RHIC*, *Phys. Rev. Lett.* **113** (2014) 052302.
- [18] ALICE collaboration, *Charge separation relative to the reaction plane in Pb-Pb collisions at $\sqrt{s_{NN}} = 2.76$ TeV*, *Phys. Rev. Lett.* **110** (2013) 012301.
- [19] CMS collaboration, *Constraints on the chiral magnetic effect using charge-dependent azimuthal correlations in pPb and PbPb collisions at the CERN Large Hadron Collider*, *Phys. Rev. C* **97** (2018) 044912.
- [20] ALICE collaboration, *Constraining the magnitude of the Chiral Magnetic Effect with Event Shape Engineering in Pb-Pb collisions at $\sqrt{s_{NN}} = 2.76$ TeV*, *Phys. Lett. B* **777** (2018) 151.
- [21] ALICE collaboration, *Constraining the Chiral Magnetic Effect with charge-dependent azimuthal correlations in Pb-Pb collisions at $\sqrt{s_{NN}} = 2.76$ and 5.02 TeV*, *JHEP* **09** (2020) 160.
- [22] STAR collaboration, *Search for the Chiral Magnetic Effect via Charge-Dependent Azimuthal Correlations Relative to Spectator and Participant Planes in Au+Au Collisions at $\sqrt{s_{NN}} = 200$ GeV*, *Phys. Rev. Lett.* **128** (2022) 092301.
- [23] STAR collaboration, *Search for the chiral magnetic effect with isobar collisions at $\sqrt{s_{NN}}=200$ GeV by the STAR Collaboration at the BNL Relativistic Heavy Ion Collider*, *Phys. Rev. C* **105** (2022) 014901.
- [24] ALICE collaboration, *Search for the Chiral Magnetic Effect with charge-dependent azimuthal correlations in Xe-Xe collisions at $\sqrt{s_{NN}} = 5.44$ TeV*, *Phys. Lett. B* **856** (2024) 138862.
- [25] STAR collaboration, *Search for the Chiral Magnetic Effect in Au+Au collisions at $\sqrt{s_{NN}} = 27$ GeV with the STAR forward Event Plane Detectors*, *Phys. Lett. B* **839** (2023) 137779.
- [26] STAR collaboration, *Upper limit on the chiral magnetic effect in isobar collisions at the Relativistic Heavy-Ion Collider*, *Phys. Rev. Res.* **6** (2024) L032005.
- [27] N. Magdy, S. Shi, J. Liao, N. Ajitanand and R.A. Lacey, *New correlator to detect and characterize the chiral magnetic effect*, *Phys. Rev. C* **97** (2018) 061901.
- [28] S.A. Voloshin, *Estimate of the signal from the chiral magnetic effect in heavy-ion collisions from measurements relative to the participant and spectator flow planes*, *Phys. Rev. C* **98** (2018) 054911.
- [29] A.H. Tang, *Probe chiral magnetic effect with signed balance function*, *Chin. Phys. C* **44** (2020) 054101.
- [30] M.M. Aggarwal, A. Attri, S. Parmar, A. Sharma and J. Singh, *Sliding dumbbell method to search for the CME in heavy-ion collisions*, *Pramana* **98** (2024) 117.
- [31] J. Schukraft, A. Timmins and S.A. Voloshin, *Ultra-relativistic nuclear collisions: event shape engineering*, *Phys. Lett. B* **719** (2013) 394.
- [32] J. Zhao, H. Li and F. Wang, *Isolating the chiral magnetic effect from backgrounds by pair invariant mass*, *Eur. Phys. J. C* **79** (2019) 168.
- [33] Z. Xu, B. Chan, G. Wang, A. Tang and H.Z. Huang, *Event shape selection method in search of the chiral magnetic effect in heavy-ion collisions*, *Phys. Lett. B* **848** (2024) 138367.
- [34] Y. Feng, Y. Lin, J. Zhao and F. Wang, *Revisit the chiral magnetic effect expectation in isobaric collisions at the relativistic heavy ion collider*, *Phys. Lett. B* **820** (2021) 136549.

- [35] W.-Y. Wu et al., *Global constraint on the magnitude of anomalous chiral effects in heavy-ion collisions*, *Phys. Rev. C* **107** (2023) L031902.
- [36] S. Shi, Y. Jiang, E. Lilleskov and J. Liao, *Anomalous Chiral Transport in Heavy Ion Collisions from Anomalous-Viscous Fluid Dynamics*, *Annals Phys.* **394** (2018) 50.
- [37] Y. Jiang, S. Shi, Y. Yin and J. Liao, *Quantifying the chiral magnetic effect from anomalous-viscous fluid dynamics*, *Chin. Phys. C* **42** (2018) 011001.
- [38] S. Shi, H. Zhang, D. Hou and J. Liao, *Signatures of Chiral Magnetic Effect in the Collisions of Isobars*, *Phys. Rev. Lett.* **125** (2020) 242301.
- [39] U.W. Heinz and J. Liu, *Pre-equilibrium dynamics and heavy-ion observables*, *Nucl. Phys. A* **956** (2016) 549.
- [40] WA98 collaboration, *Event-by-event charged-neutral fluctuations in Pb+Pb collisions at 158 A GeV*, *Phys. Lett. B* **701** (2011) 300.
- [41] R.A. Lacey and N. Magdy, *Scaling properties of the $\Delta\gamma$ correlator and their implication for detection of the chiral magnetic effect in heavy-ion collisions*, [2206.05773](#).